

**Competition between growth and shear stress  
drives intermittency in preferential flow paths in porous media biofilms**

Dorothee L. Kurz<sup>1,2</sup>, Eleonora Secchi<sup>1\*</sup>, Francisco J. Carrillo<sup>3</sup>, Ian C. Bourg<sup>4</sup>, Roman Stocker<sup>1</sup>, Joaquin Jimenez-Martinez<sup>1,2\*</sup>

(1) Institute of Environmental Engineering, Department of Civil, Environmental and Geomatic Engineering, ETH Zurich, Zurich, Switzerland

(2) Department Water Resources and Drinking Water, Swiss Federal Institute of Aquatic Science and Technology, Eawag, Dübendorf, Switzerland

(3) Department of Chemical and Biological Engineering (CBE), Princeton University, Princeton, NJ, USA

(4) Department of Civil and Environmental Engineering (CEE) and High Meadows Environmental Institute (HMEI), Princeton University, Princeton, NJ, USA

\* To whom correspondence may be addressed: Eleonora Secchi, Joaquin Jimenez-Martinez

**Email:** esecchi@ethz.ch; joaquin.jimenez@eawag.ch

PNAS strongly encourages authors to supply an [ORCID identifier](#) for each author. Do not include ORCIDs in the manuscript file; individual authors must link their ORCID account to their PNAS account at [www.pnascentral.org](http://www.pnascentral.org). For proper authentication, authors must provide their ORCID at submission and are not permitted to add ORCIDs on proofs.

**Author Contributions:** D.K., E.S., R.S., and J.J.M. designed research; D.K. and E.S. performed the experiments; F.C. and I.B. designed and built the mathematical model; D.K., E.S., F.C. and J.J.M. analyzed data; and D.K., E.S., F.C., I.B., R.S. and J.J.M. wrote the paper.

**Competing Interest Statement:** The authors declare no competing interest.

**Classification:** Physical Sciences – Environmental Sciences

**Keywords:** bio-clogging, biofouling, bacterial biofilms, porous media flow, biofilm dynamics.

**This PDF file includes:**

Main Text  
Figures 1 to 5

2 **Abstract**

3 Bacteria in porous media, such as soils, aquifers and filters, often form surface-attached  
4 communities known as biofilms. Biofilms are affected by fluid flow through the porous  
5 medium, for example for nutrient supply, and they in turn affect the flow. A striking  
6 example of this interplay is the strong intermittency in flow that can occur when biofilms  
7 nearly clog the porous medium. Intermittency manifests itself as the rapid opening and  
8 slow closing of individual preferential flow paths (PFPs) through the biofilm–porous  
9 medium structure, leading to continual spatio-temporal rearrangement. The drastic  
10 changes to the flow and mass transport induced by intermittency can affect the  
11 functioning and efficiency of natural and industrial systems. Yet, the mechanistic origin of  
12 intermittency remains unexplained. Here, we show that the mechanism driving PFP  
13 intermittency is the competition between microbial growth and shear stress. We  
14 combined microfluidic experiments quantifying *Bacillus subtilis* biofilm formation and  
15 behavior in synthetic porous media for different pore sizes and flow rates with a  
16 mathematical model accounting for flow through the biofilm and biofilm poroelasticity to  
17 reveal the underlying mechanisms. We show that closing of PFPs is driven by microbial  
18 growth, controlled by nutrient mass flow. Opposing this, we find that the opening of PFPs  
19 is driven by flow-induced shear stress, which increases as a PFP becomes narrower due  
20 to microbial growth, causing biofilm compression and rupture. Our results demonstrate  
21 that microbial growth and its competition with shear stresses can lead to strong temporal  
22 variability in flow and transport conditions in bio-clogged porous media.

23 **Significance Statement**

24 Biofilms are ubiquitous in porous media, including in soils and technical applications  
25 such as bioremediation and wastewater treatment systems. Biofilms can drastically alter  
26 the transport of nutrients and contaminants through porous media by forming preferential  
27 flow paths, which are subject to strong intermittency in fluid flow. This intermittency  
28 manifests through the opening and closing and spatio-temporal rearrangement of flow  
29 paths, and its mechanism has to date remained unresolved. Here we show that  
30 intermittency is driven by the competition between microbial growth that governs the  
31 closing of preferential flow paths and biofilm compression and rupture that controls their  
32 opening.

33  
34 **Main Text**

35 **Introduction**

36 Porous media often constitute an ideal habitat for the formation of bacterial biofilms, both  
37 in the environment and in technological and medical settings. Biofilms in porous media  
38 contribute to enhancing reaction rates in biomineralization, bioremediation, enhanced oil  
39 recovery, water treatment, and biochemical production (1–4), but also have major  
40 negative impacts in medical and filtration applications, where they cause clogging.  
41 Within biofilms, bacteria embed themselves in a secreted matrix of extracellular  
42 polymeric substances mainly consisting of lipids, exopolysaccharides, proteins, and  
43 extracellular DNA (5–7). This gel-like matrix protects the bacteria from nutrient  
44 fluctuations, dehydration, and mechanical and chemical insults (7, 8). The matrix also  
45 has a structural role, as its composition determines the biofilm's rheological properties  
46  
47

48 (6, 7, 9), which are crucial in controlling the detachment and spatial rearrangement of  
49 biomass when exposed to shear stresses (10). Biofilms have a complex rheology, which  
50 has been described as viscoelastic (9, 11) or viscoplastic behavior (12), and which  
51 confers on them the ability to retain their structure while undergoing shear-induced  
52 deformation. Biofilm morphology depends on flow conditions: in the absence of flow  
53 (e.g., on agar plates) bacteria form compact biofilm colonies, sometimes crossed by  
54 channels (13), whereas under flow, bacteria form dense, layered biofilms (14) or  
55 suspended filaments known as streamers (15).

56  
57 Within porous media, biofilms are exposed to a wide range of fluid flow velocities (16).  
58 They form through several characteristic stages: initial attachment of cells to the solid  
59 surfaces of the porous medium, the formation of clusters and streamers, and finally the  
60 clogging of pore spaces (17). Biofilm development is driven by the balance of  
61 attachment (18), growth, and detachment (19). While bacterial transport through porous  
62 media is mainly controlled by the flow field (20–22), the spatial distribution of biofilm is  
63 additionally governed by shear forces, which influence bacterial transport and thereby  
64 determine initial bacterial attachment (23). The production of extracellular polymeric  
65 substances by biofilms, their matrix structure and thereby their macroscopic appearance  
66 are a function of the interplay between hydrodynamics and nutrient availability (24, 25).  
67 As they grow, biofilms cause bio-clogging, reducing the porosity (26) and the hydraulic  
68 conductivity (27) of the porous medium. Experimental studies and numerical models  
69 have shown that under conditions in which a given flow rate is imposed, biofilms can  
70 lead to the formation of preferential flow paths (PFPs) through the composite structure  
71 made by the porous medium and the biofilm. They also reveal the emergence of  
72 recurrent opening and closing behavior of the PFPs, resulting in intermittency (2, 28, 29).  
73 Studies to date have been limited to a single porous geometry (2, 28, 30) and have  
74 relied on the simplified assumption of a constant cell decay (29). Therefore, a  
75 mechanistic understanding of the intermittent opening and closing of PFPs and their  
76 spatio-temporal rearrangement in biofilms has been missing.

77  
78 Here, we report experiments and mathematical simulations of fluid flow through a  
79 biofilm–porous medium structure and show that the mechanism for intermittency is the  
80 competition between microbial growth that closes flow paths and flow-induced stress  
81 that opens them abruptly through compression and rupture of the biofilm. Using  
82 microfluidic experiments that combine imaging at high temporal and spatial resolution  
83 and direct pressure measurements, together with mathematical simulations based on  
84 the Darcy–Brinkman–Biot model, we systematically studied biofilms in porous media for  
85 a range of flow rates and pore sizes. Our results reveal that the coupling between fluid  
86 flow and microbial growth can drastically alter transport properties in bio-clogged porous  
87 media, with far-reaching implications for the distribution of nutrients and contaminants.

88  
89 **Results**  
90

91 **Preferential flow path intermittency in bio-clogged porous media.** While studying  
92 biofilm development by the wild-type bacterium *Bacillus subtilis* within model porous  
93 media, we observed reproducible formation of preferential flow paths (PFPs) and strong  
94 intermittency in their opening and closing. Porous media were formed by a microfluidic  
95 device containing an array of pillars with diameter and spacing between pillars (the pore  
96 size,  $d$ ) of 300  $\mu\text{m}$  for the initial experiments, in an array measuring 22 mm  $\times$  4.05 mm

97 with height 100  $\mu\text{m}$  (Fig. 1A; *Materials and Methods*). The initial porosity of this model  
98 medium was 0.77. Flow of a nutrient solution (for details of composition see *Materials*  
99 and *Methods*) was imposed with a flow rate,  $Q$ , of 1 mL/h. Within such a system, the  
100 vertical velocity profile at a given position is controlled by the distance between the two  
101 nearest pillars (31). In our device, this distance was of the same order as the height: this  
102 results in a quasi-2D flow, where the vertical profile of the horizontal velocity,  $v_x(z)$ , is  
103 intermediate between the parabolic profile expected for a lower model height and the  
104 plug-flow profile with narrow limit boundaries at the top and bottom boundaries expected  
105 for a higher model height (32). After loading the bacterial culture into the microfluidic  
106 device and initial attachment of individual bacteria (Fig. 1B), biofilms formed on the  
107 pillars as clusters (surface-attached chunks of biofilm; white outline, Fig. 1C), and  
108 streamers (biofilm suspended in the flow; orange outline, Fig. 1C). Further growth  
109 resulted in complete clogging of most pores after 20 h (Figs. 1D and E). In the bio-  
110 clogged porous medium, we observed preferential flow paths (PFPs). PFPs consisted of  
111 biofilm-free channels forming an often-tortuous path through the biofilm–porous medium  
112 structure, spanning the length of the system (highlighted in yellow in Figs. 1F–H). PFPs  
113 were seen to branch (blue circle, Fig. 1F) and coalesce (green circle, Fig. 1F). The  
114 position of PFPs changed over time until a steady geometrical configuration was  
115 reached after about 35 h (*SI Appendix*, Fig. S1).

116 The bio-clogged porous medium exhibited strong intermittency in the opening and  
117 closing of preferential flow paths. To quantify changes in PFP width over time, we used  
118 high-resolution bright-field imaging ( $13500 \times 2500$  pixels acquired at  $4\times$  magnification)  
119 from 16 locations spanning the entire porous domain. We calculated the mean PFP  
120 width,  $w$ , by measuring width along the PFP and averaging over 6 min time windows,  
121 between 24 h and 45 h (*Materials and Methods*). We found that PFP width varied over  
122 time, between 50  $\mu\text{m}$  and 110  $\mu\text{m}$  (Fig. 1I). This intermittent opening and closing  
123 behavior occurred while the PFPs were still varying in position as well as when the PFPs  
124 were in a steady position.

125 To characterize PFP intermittency, we measured the pressure difference,  $\Delta p$ , between  
126 the inlet and the outlet of the microfluidic device using pressure sensors (*Materials and*  
127 *Methods*). Comparison of the temporal changes in the pressure difference,  $\Delta p$ , and in  
128 the PFP width,  $w$ , revealed that opening and closing events correlated with changes in  
129 pressure difference (Fig. 1I, e.g., at  $t = 33.8$  h,  $t = 35.2$  h). Narrowing of the mean PFP  
130 width resulted in an increase in the pressure difference (Fig. 1I). The increased pressure  
131 difference was due to a reduction in the hydraulic conductivity of the system (according  
132 to Darcy's law). Similarly, the opening of the PFPs resulted in an increase in  $w$  and a  
133 decrease in the pressure difference (Fig. 1I). Further, a gradual increase of the pressure  
134 difference was observed in time. The timescales of opening and closing were very  
135 different: closing of the PFPs was a gradual process that took 2–5 h, whereas the  
136 opening of the PFPs was extremely rapid, completed below the temporal resolution of  
137 the image acquisition, on a timescale of 0.2–2 s (*SI Appendix*, Movie S1).

138 **Microbial growth drives flow path closing, hydromechanical processes drive their**  
139 **opening.** A systematic analysis of PFP formation and quantitative investigation of PFP  
140 opening and closing enabled us to determine the biological and hydromechanical  
141 mechanisms controlling PFP intermittency.

142 The long timescale of PFP closing (2–5 h) suggested that the process was driven by  
143 microbial growth. To test this hypothesis, we switched the flow of the medium provided  
144 to a mature biofilm from the nutrient solution to an isotonic salt solution. This switch  
145 deprived the cells of nutrients and thus suppressed growth, without altering the osmotic  
146 pressure to avoid any change in shape or stiffness of the biofilm. A halt in previously  
147 observed intermittency was observed in the porous medium exposed to the flow of  
148 isotonic salt solution (Fig. 2A), confirming that microbial growth is necessary for  
149 intermittency. We infer from this that growth is responsible for the closing of PFPs, which  
150 is confirmed by the fact that no closing of PFPs was observed during the flow of the  
151 isotonic salt solution (Fig. 2A). We further note that no detachment was observed in this  
152 experiment, suggesting that starvation associated with the lack of nutrients does not  
153 cause an increase in biomass decay on the timescale of these observations (24 h).

154 The rapidity of PFP opening in contrast, in the order of 0.2 to 2 s (*SI Appendix*, Movie  
155 S1), led us to hypothesize that opening was driven by a physical process, and  
156 specifically by the shear forces associated with flow through the biofilm. As PFPs  
157 become narrower due to microbial growth, the same flow rate passing through the PFPs  
158 induces a stronger shear force. In order to test the hypothesis that this shear controls  
159 PFP opening, we recorded 1-hour-long phase-contrast microscopy videos (10×  
160 objective) at high speed (20 frames/s) to capture the details of the very rapid opening  
161 events. From the videos, we tracked biofilm movement using digital image correlation  
162 (DIC) (33). DIC is an optical method that employs a tracking technique and cross-  
163 correlation to measure changes in the pixels of images. This analysis allowed us to  
164 identify the direction of movement of microscale regions of the biofilm adjacent to PFPs  
165 and thus quantify structural changes associated with PFP opening.

166 Based on this analysis, we identified two processes driving PFP opening (*SI Appendix*,  
167 Movie S1, Fig. 2 B and C). The first process was sloughing off of biofilm, in which large  
168 parts of the biofilm directly bordering a PFP detached and were flushed out through the  
169 PFP. A sloughing-off event was identified from the videos as a portion of biofilm  
170 suddenly disappearing from the image sequence (Fig. 2B). The area of the biofilm  
171 bordering the PFP mainly affected by the sloughing off displayed a lighter gray color  
172 compared to the layers of the biofilm further away from the PFP, the denser layer (Fig.  
173 2B). The second process was the compression of regions of the biofilm directly adjacent  
174 to a PFP and the associated movement of the biofilm structure perpendicular to the PFP,  
175 resulting in widening of the flow path. Compression was detected from the DIC analysis  
176 of the videos as the local movement of the biofilm moving away perpendicularly from the  
177 PFP (Fig. 2C). During compression, the biofilm structure moved at speeds in the order of  
178  $10^{-2}$  mm/s, which is one order of magnitude lower than the initial mean flow velocity.

179 PFP closing causes an increase in the shear rate within the PFP, which is released upon  
180 a PFP opening event. To analyze the evolution of shear rate in the PFPs we performed  
181 numerical simulations of the fluid flow velocity based on the experimental images of Fig.  
182 1F–H and Fig. 2B, C using COMSOL Multiphysics (*SI Appendix*). We validated these  
183 flow simulations using experimental particle image velocimetry (PIV) data (*SI Appendix*,  
184 Fig. S3). From the numerical simulations, we quantified both the shear rates and the  
185 normal forces acting on the boundaries of the PFP. The shear rate distribution in the  
186 PFPs for the entire biofilm–porous-medium domain depends on the state of the PFPs  
187 (Fig. S2): in an open PFP, the probability density function of the shear rate peaks at  
188 lower values compared to those in a narrow PFP. This result confirms that PFP opening

189 events cause the shear rate to decrease, which conversely increases in the PFP during  
190 their narrowing. From a pore-scale perspective, we numerically computed the velocity  
191 field and shear rates based on the images of Fig. 2B (Fig. 2D, F). Before the sloughing  
192 of the biofilm fragment responsible for narrowing the PFP in Fig. 2B (circled in black), the  
193 shear rates at the biofilm interface were two orders of magnitude higher compared to  
194 those in the open PFP (Fig. 2F). Additionally, we computed the force acting  
195 perpendicular to the biofilm walls at the boundary of the PFP, finding that the biofilm  
196 deformation occurs perpendicular to the mean flow direction and that the normal force  
197 decreases downstream (Fig. 2G), thus confirming the role of compression in opening of  
198 PFPs.

199 **A mathematical model supports the dependence of PFP intermittency on biofilm  
200 growth and hydrodynamic stress.** To further investigate the physical and biological  
201 mechanisms of PFP intermittency, we developed a new mathematical model of biofilm  
202 formation in porous media based on a Darcy–Brinkman–Biot formulation used to model  
203 flow within and around deformable porous media (34, 35), yet never applied to biofilms.  
204 The model resolved flow through the biofilm and represented the biofilm as a  
205 viscoplastic continuum (12). The model included both flow in the PFPs and through the  
206 matrix of the biofilm, with the former described by Stokes flow (the inertial terms of the  
207 Navier–Stokes equation are negligible) and the latter represented using Darcy's law and  
208 Biot poromechanics. The following assumptions were made in the model: (i) biofilm  
209 growth can be approximated as a first-order reaction obeying the mass conservation law  
210 (36); (ii) the biofilm behaves as a viscoplastic material, meaning that it deforms viscously  
211 only after the shear stress on the biofilm exceeds the critical yield stress (12), and (iii) all  
212 biofilm properties are independent of porosity, except for permeability, viscosity, and  
213 yield stress. These assumptions allow solution of the hydrodynamics within the biofilm  
214 and capture of the biofilm growth process, without the use of fitting parameters.  
215 Technical details of the model and the assumptions can be found in *SI Appendix*.

216 No fitting parameters were used for the model. The model reproduces PFP formation  
217 and the intermittency phenomenon. For a model porous domain similar to the  
218 experimental system (5 mm × 4 mm, containing pillars of diameter 300  $\mu\text{m}$  in an array  
219 with spacing 300  $\mu\text{m}$ ), the model yielded a very similar opening and closing behavior  
220 (Fig. 3 A–C), replicating the spatio-temporal dynamics of biofilm behavior within the  
221 microfluidic model system. We compared model and experimental results quantitatively  
222 by investigating the evolution over time of the mean PFP width,  $w$  (Fig. 3D). The mean  
223 PFP width predicted by the model fluctuated around 100  $\mu\text{m}$  and varied between 65 and  
224 130  $\mu\text{m}$ , in a manner comparable to the experimental data (Figs. 3D and 1I). As in the  
225 experiments, the model results showed that the increase in PFP width was very rapid,  
226 whereas the closing was slow (Fig. 3D).

227 The model results confirm that intermittency is controlled by the interplay between  
228 microbial growth and shear stresses (*SI Appendix*, Fig. S5). Eliminating microbial growth  
229 during a model run resulted in the intermittency disappearing, as evidenced by the near  
230 constancy of the mean PFP width (Fig. 3D, blue curve). The small residual fluctuations  
231 in PFP width were considered noise, as their magnitude was considerably lower than the  
232 changes in  $w$  caused by intermittency. Therefore, the halt in PFP intermittency without  
233 microbial growth in the model confirmed the experimental result in which suppression of  
234 growth had the effect of eliminating intermittency (Fig. 2A). Additionally, decreasing the  
235 fluid flow rate (and thus the fluid flow velocity and shear rate) in the model led to a fully

236 bio-clogged system: PFPs entirely disappeared (note that fluid flow can still occur  
237 through the biofilm due to its porosity). This modeling result shows that removing the  
238 shear stresses exerted by the fluid flowing in the PFPs resulted in the disappearance of  
239 intermittency, confirming the experimental observations on the role of flow in causing the  
240 opening of PFPs (Figs. 2 B and C).

241  
242 **Intermittency occurs for high fluid flow velocities and large pore sizes.** To  
243 investigate the influence of pore size and fluid flow velocity on the emergence of PFP  
244 intermittency, we repeated experiments in microfluidic devices with three different values  
245 of pore size,  $d = 75, 150$  and  $300\text{ }\mu\text{m}$  (Fig. 4A), all with the same porosity (0.77). For  
246 each pore size, experiments were performed at four different flow rates,  $Q$ : 0.2, 0.5, 1  
247 and 2 mL/h. The corresponding mean fluid flow velocities can be found in *SI Appendix*,  
248 Table S5. For a given fluid flow rate, the mean fluid velocity was the same in the three  
249 devices with different pore sizes, because their porosity was the same. In contrast, the  
250 local shear force within the porous medium increases with decreasing pore size (Fig.  
251 4A).

252 In mature biofilms that developed within these porous media, we found that larger pore  
253 size led to larger mean PFP width,  $w$  (Fig. 4B and *SI Appendix*, Fig. S6). This, in turn,  
254 resulted in a lower pressure difference across the microfluidic device (*SI Appendix*, Fig.  
255 S7A). In general, for the conditions investigated, the mean PFP width at maximal  
256 opening was approximately half of the pore size (Fig. 4B): for example, at the pore size  
257 of  $300\text{ }\mu\text{m}$ , PFPs had a maximal mean width of about  $150\text{ }\mu\text{m}$ . The fact that the maximal  
258 mean PFP width was about half the pore size indicates that some stable biofilm structure  
259 remained in the pores while the PFPs were open. Therefore, we conclude that for the  
260 range of experimental conditions investigated, parts of the biofilm were sufficiently stable  
261 to withstand the shear forces causing PFP opening. As described above for the largest  
262 pore size of  $300\text{ }\mu\text{m}$ , for the other conditions studied the PFP width,  $w$ , and the pressure  
263 difference,  $\Delta p$ , also varied through time and were inter-dependent (Figs. 1F–I and *SI*  
264 *Appendix*, Fig. S7). We found that the relationship between  $\Delta p$  and  $w$  can be described  
265 by a power law,  $\Delta p = a \cdot w^{-b}$ , with  $a$  and  $b$  depending on the flow velocity and the pore  
266 size (*SI Appendix*, Fig. S7). In order to place our results in a hydrodynamic context, we  
267 compared the experimentally obtained PFP width,  $w$ , and corresponding pressure  
268 difference,  $\Delta p$ , with the analytical solutions for fluid flow through an equivalent  
269 rectangular pipe with width equal to the average width of the PFPs (Hagen–Poiseuille  
270 law,  $\Delta p \sim w^{-2.4}$  (37)) and through a porous domain of the size of the microfluidic device  
271 (Darcy's law,  $\Delta p \sim w_{pd}^{-1}$ , where  $w_{pd}$  is the width of the porous domain (38)) (*SI*  
272 *Appendix*, Table S2). We found that our experimental data lie between the two analytical  
273 solutions, i.e., with  $1 < b < 2.4$  (*SI Appendix*, Fig. S7), meaning that the flow through a  
274 bio-clogged porous medium containing PFPs can be described as the combination of the  
275 flow through a pipe and the flow through a continuum domain described by Darcy's law.  
276 The bio-clogged system thus consists of a dual-porosity domain having macropores  
277 (PFPs) and a porous matrix (biofilm).

278 Experiments revealed that the occurrence of intermittency depended on both the pore  
279 size and the fluid flow rate. Based on the experimental results for different pore sizes  
280 and fluid flow rates, we constructed a phase diagram representing the regimes in which  
281 intermittency occurs (Fig. 4C). For this, we define intermittency as the presence of PFPs  
282 that show repeated changes in width of  $5\text{ }\mu\text{m}$  between narrow and opened paths. The

283 phase diagram displays two regions. Flow path intermittency was observed in the upper-  
284 right region, for high fluid flow rates and large pore sizes (Fig. 4C, green region), while it  
285 was absent (Fig. 4C, red region) at the lowest fluid flow rate tested (0.2 mL/h) for all pore  
286 sizes, and also for a flow rate of 0.5 mL/h at the smallest pore size (75  $\mu\text{m}$ ).

287 **Characterizing PFP closing speed and opening frequency.** For PFP intermittency to  
288 occur, the biofilm must first clog the individual pores. Once the PFPs are formed, the  
289 biofilm must experience sufficient shear to open the PFPs by sloughing and  
290 compression, while continuing to grow. In order to quantify the timescale of clogging of  
291 individual pores, we computed the pore clogging speed,  $v_c$ , for the range of flow rates  
292 and pore sizes studied using the Gompertz growth model (*Materials and Methods* and *SI*  
293 *Appendix*, Figs. S8 and S9). We found that the mean pore clogging speed,  $v_{mc}$ ,  
294 increases with increasing fluid flow rate,  $Q$ , and pore size,  $d$  (Fig. 5A). We observed PFP  
295 intermittency (stars in Fig. 5A) under conditions that supported high pore clogging  
296 speed. We further explore the link between pore clogging speed and two parameters  
297 related to fluid flow velocity and pore size: (i) the shear rate and (ii) the nutrient mass  
298 flow per pore. In our experiments, the pore clogging speed correlated with the relative  
299 nutrient mass flow per pore, calculated by dividing the imposed flow rate by the number  
300 of pore throats orthogonal to the flow direction for each microfluidic device and  
301 normalizing by the maximal nutrient mass flow rate (Fig. 5B). Pore clogging speed  
302 during the early stages of biofilm growth can be described by Monod kinetics adapted to  
303 our parameters as

$$v_{mc} = v_{\max} \frac{S}{S + K_N} \approx v_{mc,\max} \left( \frac{M}{M + K_N \cdot Q} \right), \quad \text{Eq. 1}$$

304 with  $v_{\max}$  the maximum growth rate,  $S$  the nutrient concentration,  $K_N$  the half-saturation  
305 constant,  $M$  the relative nutrient mass flow per pore,  $Q$  the imposed fluid flow rate, and  
306  $v_{mc,\max}$  the maximal pore clogging speed of all experimental conditions. The Monod  
307 kinetic model describes the dependence of cellular growth on the availability of nutrients  
308 (39). Similarly, as the closing of the PFPs depends on biofilm growth, we found that the  
309 mean PFP closing speed,  $M_{PFP}$ , also follows Monod kinetics as a function of the relative  
310 nutrient mass flow rate (Eq. 1) (Fig. 5C). However, the curve for PFP closing speed  
311 reaches a lower plateau for the maximum closing speed compared with the behavior of  
312 individual pores. In contrast to the PFP closing speed, the pore clogging speed was  
313 measured in the early stages of the porous medium clogging and prior to PFP formation,  
314 so that the lower maximal value for the PFP closing speed is likely explained by a higher  
315 shear stress in the PFP compared to that in the individual pores during the initial stages  
316 of clogging. These correlations of PFP closing speed and individual pore clogging speed  
317 with the relative nutrient mass flow are in accordance with our conclusion from the  
318 nutrient removal experiment (Fig. 2A) that the mechanism for PFP closing is biofilm  
319 growth. The mean pore-clogging speed and the mean PFP closing speed both reach a  
320 plateau at high relative nutrient mass flow rate (Fig. 5B, C), suggesting that the growth at  
321 different stages of the clogging process is limited by some environmental factor.  
322 However, massive biofilm dispersal was never observed in the experiment, confirming  
323 that the supplied nutrients are sufficient to sustain biofilm survival.

324 As PFP opening was driven by a hydromechanical mechanism related to shear forces,  
325 we hypothesized that the frequency of PFP opening,  $F$ , would correlate with the shear  
326 rate. In our experiments, we indeed observed a positive correlation between the average

327 shear rate in the PFP and  $F$  (Fig. 5D). The shear rate,  $\dot{\gamma}_w$ , acting on the PFP walls was  
328 computed as

$$\dot{\gamma}_w = 8 \cdot Q / D_h \cdot h \cdot \bar{w}, \quad \text{EQ. 2}$$

329 With  $Q$  the imposed flow rate,  $D_h$  the hydraulic diameter of the PFP,  $h$  the height of the  
330 microfluidic device, and  $\bar{w}$  the mean width of the PFP during each experiment (40),  
331 obtained by averaging the PFP width over the entire duration of one experiment (24 h).  
332 This estimate of the shear rate relies on the assumption that all of the fluid flow passes  
333 through the PFP (as demonstrated by numerical simulations, *SI Appendix*, Fig. S2B) and  
334 we have a no-slip condition at the PFP walls, owing to the low permeability of the biofilm  
335 a no-slip condition at the PFP wall, owing to the low permeability of the biofilm ( $10^{-14} \text{ m}^2$ ,  
336 *SI Appendix*). The analysis of opening frequency showed that  $F$  increased with the shear  
337 rate up to a value of shear rate of  $1.2 \times 10^4 \text{ s}^{-1}$ , at which point  $F$  stabilized around  $0.7 \text{ h}^{-1}$   
338 (Fig. 5D). This result indicates that larger fluid flow rates and smaller mean PFP widths  
339 maximize and stabilize the opening frequency.

## 340 Discussion

341

342 Our work has elucidated the mechanism underlying PFP intermittency in biofilm-bearing  
343 porous media and has shown that intermittency is due to the competition between  
344 microbial growth and fluid shear stress. Closing of the PFPs is controlled by the nutrient  
345 mass flow: in an experiment in which flow contained no nutrients, intermittency ceased  
346 completely. Opening of the PFPs, due to detachment of the biofilm and its compression  
347 normal to the direction of flow, results from the viscoelastic mechanical behavior of the  
348 biofilm under shear stress (41). Using a mathematical model based on the Darcy–  
349 Brinkman–Biot formulation, we confirmed that suppressing biofilm growth or decreasing  
350 the shear stress exerted by the fluid flow halted PFP intermittency.

351 To compare the dynamics of PFP closing to that of the clogging of individual pores, we  
352 characterized individual pore clogging using the extended Gompertz growth model,  
353 extensively used to describe both bacterial growth in bulk (42) and biofilm growth under  
354 flow (43). We found that biofilm growth dynamics appear to be maintained in porous  
355 media both at the pore scale and during clogging of the entire system, despite the shear  
356 forces to which the biofilm is exposed. When comparing the plateaus of the Monod fits  
357 for the clogging of individual pores and for the closing of PFPs, we found that the  
358 maximal PFP closing speeds were an order of magnitude smaller than the maximal  
359 individual pore clogging speeds. This is likely explained by differences in the shear rate,  
360 which is much higher in PFPs as the porous medium approaches full clogging than in  
361 individual pores in the early stages of clogging. The shear rates in a microfluidic device  
362 of pore size  $d = 300 \mu\text{m}$ , at a flow rate  $Q = 1 \text{ mL/h}$  range from  $10^1$  to  $10^3 \text{ 1/s}$  in the early  
363 stage (Fig. 4A), whereas in a PFP shear rates are estimated to range from  $10^4$  to  $10^6 \text{ 1/s}$   
364 (Fig. 2F). Once PFPs have formed, most of the fluid flow is channeled through the open  
365 paths, since very little flow can be accommodated by the biofilm due to its very low  
366 permeability (13).

367 Biofilm sloughing off within porous media leading to the rapid opening of PFPs will affect  
368 downstream clogging, as the flow transports chunks of biofilm and individual bacterial  
369 cells. Mass transport and the regaining of cell motility can lead to subsequent spreading  
370 of bacteria within a pore network (44, 45). The occurrence of detachment is determined

371 by fluid flow, nutrient supply and the geometry of the habitat, but also by the mechanical  
372 properties of the biofilm (41, 46). The mechanical properties of the biofilm can vary in  
373 space and time depending on the depth (normal to the direction of the preferential flow  
374 path) into the biofilm. In space, we observed a gradual increase in density (i.e., a  
375 decrease of light intensity) deeper into the biofilm. In time, we observed a gradual  
376 increase of pressure in the successive closing-opening cycles of the PFP. Further, the  
377 elastic properties allow the biofilm to withstand disturbances shorter than the elastic  
378 relaxation time, while longer stress will lead to non-reversible viscoplastic deformation,  
379 sloughing and detachment (47). In our experiments, we observed that the biofilm was  
380 sloughed off intermittently. This hints at a non-Newtonian behavior: a critical shear stress  
381 is required to overcome the yield stress of the biofilm in order to trigger PFP  
382 intermittency. These results have an abiotic analogy in cohesive sediment transport,  
383 where a critical shear stress is required to induce sloughing (48). In natural settings,  
384 biofilms in sediments can prevent sediment erosion, thanks to the yield stress of the  
385 biofilm (49, 50). In order to capture biofilm behavior in models of porous media, it is  
386 crucial to take the mechanical properties of the biofilm into account. In our study, we  
387 modeled the biofilm as a viscoplastic material with a yield stress, which allowed us to  
388 reproduce the intermittent PFP behavior. The viscoplastic behavior captures the  
389 observed, intermittent sloughing off better than a viscoelastic behavior, which would  
390 imply greater flowing of the biofilm rather than detachment.

391 The rheological properties of the biofilm depend on the composition of the extracellular  
392 polymeric substances, which, in turn, can vary greatly depending on the microorganisms  
393 present, the nutrient availability, and the environmental conditions (51). The interplay  
394 between biofilm rheology and local flow conditions determines biofilm morphology, as  
395 recently demonstrated (52). In particular, our results show that the biofilm's viscoplastic  
396 behavior drives its capability of clogging and forming preferential flow paths in a porous  
397 medium, as the rheological descriptors of the biofilm were critical parameters of the  
398 mathematical model we developed. We hypothesize that a change in biofilm rheology,  
399 for example due to the presence of a different bacterial species or a drastic shift in  
400 environmental conditions, may affect the occurrence of PFP intermittency and the  
401 frequency of opening and closing events. Furthermore, fast-growing bacterial  
402 communities are more efficient in clogging porous structures and will consequently  
403 reduce their access to flowing nutrients, so that slow-growing competitors may be  
404 favored (53). Similarly, the occasional sloughing will increase access to nutrients by  
405 avoiding flow paths from being choked off, thus promoting bacterial growth locally. This  
406 implication is counter to the implied consensus in the literature that more robust biofilms  
407 or stronger biofilm growth are always beneficial to bacteria growing on surfaces under  
408 shear stress, and may imply that biofilms can tune their physical properties depending  
409 on cell density and access to nutrient supply in order to promote survival.

410 The intermittent opening and closing of the PFPs was reflected in the pressure  
411 difference through the system: closing of the PFPs resulted in an increase in the  
412 pressure difference due to a reduction in the bulk hydraulic conductivity of the system,  
413 whereas opening of the PFPs reduced the pressure difference. We observed this  
414 behavior for completely clogged porous media: this stands in contrast to bio-induced  
415 partial clogging of a porous medium, where the continuous reduction in pressure  
416 difference results mainly from biofilm formation in the upstream part of the porous  
417 medium (2). From this, it can be concluded that observation of a recurring pressure  
418 increase and decrease within a porous medium cannot solely be attributed to

419 breakthrough of a bio-induced plug, but can also be due to intermittent PFPs. We  
420 demonstrated that a power law with a negative exponent that falls between the Hagen–  
421 Poiseuille and Darcy solutions best describes the relation between pressure difference  
422 and PFP width.

423 Our systematic study of the dependency of PFP intermittency on fluid flow rate and pore  
424 size expands and generalizes the conditions under which PFP intermittency is known to  
425 occur (28, 29). We showed that intermittency occurs only under certain conditions, at  
426 fluid flow rates larger than 0.5 mL/h and pore sizes larger than 75  $\mu\text{m}$ . Whether PFP  
427 intermittency occurs can be explained by the impact of fluid shear stresses in  
428 combination with the material properties of the biofilm. We observed an increasing  
429 frequency of opening of PFPs with increasing shear forces, which cause more biofilm  
430 detachment (19, 29). We observed a stabilization in the frequency of PFP opening over  
431 time. We attribute this to a more stable biofilm structure over time because of a  
432 densification deeper into the biofilm due to compression and the regular removal by  
433 shear of the newly formed biofilm closest to the PFP (*SI Appendix*, Movie S1). The PFP  
434 closing speed correlated with the nutrient mass flow rate and followed a Monod kinetic,  
435 as we also observed for the clogging speed of individual pores. Weak or no PFP  
436 intermittency was observed at low flow rates because no PFPs were formed. Instead,  
437 complete bio-clogging was observed. For the smallest pore size, in contrast, a PFP was  
438 formed due to a catastrophic rupturing, but without subsequent intermittent opening and  
439 closing (*SI Appendix*, Fig. S10). This is likely explained by the larger surface for biofilm  
440 attachment with smaller pore size, which allows the biofilm to form a denser and more  
441 rigid network. The biofilm can thus withstand higher pressures, until it abruptly ruptures  
442 and forms a large flow path without intermittency (*SI Appendix*, Fig. S10).

443 By combining microfluidic experiments and mathematical modeling, we were able to  
444 unravel the competing mechanisms driving PFP intermittency, and fully characterize  
445 PFP behavior under a range of geometric and hydraulic conditions relevant in  
446 environmental sciences and industrial technologies such as filters and bioreactors. In our  
447 microfluidic devices, the grains are regularly arranged and all pores have the same initial  
448 fluid flow conditions. Despite this scenario being a simplification of the irregular nature of  
449 soils, it allowed a systemic study of pore clogging and an unprecedented comparison of  
450 different hydrodynamic conditions. In our experiments, the fluid flow rates ranged from  
451 0.2 to 2 mL/h (corresponding to velocities of 16 to 160 m/d), which are comparable to  
452 transport velocities of microorganisms in soils (54) and in bioremediation applications  
453 (55). In addition to determining the effect of irregular grain arrangements on  
454 intermittency, it will be interesting to study how intermittency changes when one  
455 considers pressure-driven flow, common in natural environments, rather than an  
456 imposed flow rate as done here. Additionally, we highlight that imposed flow is found in  
457 certain technical applications, including biomimetic mineralization (56) and biochemical reactors  
458 (57) and that our experimental fluid flow velocities are of the same order of magnitude as  
459 in those applications. The formation and dynamics of PFPs in porous media strongly  
460 impact mass transport by creating spontaneous chemical inundations during PFP  
461 opening. Each opening results in a rapid change of the velocity distribution in the  
462 biofilm–porous medium system, leading to a transient flow system with high variance in  
463 residence time and strong mixing of chemicals with resident solutions, hence increasing  
464 the efficiency of reactions (58). PFP intermittency, a phenomenon based on the interplay  
465 between hydromechanical and biological processes, can be relevant in natural and  
466 industrial systems, with applications ranging from soil and aquifer bioremediation,

467 bioreactors, filtration (design of membranes), and enhanced oil recovery. Our findings  
468 can contribute to improving the understanding of natural systems and assist in the  
469 design of applications that harness the properties of biofilms.

470  
471 **Materials and Methods**  
472

473 **Microfluidic device design.** Microfluidic devices were used to enable imaging of biofilm  
474 formation in a controlled environment at very high spatial and temporal resolution (59).  
475 Cylindrical polydimethylsiloxane (PDMS) pillars in the microfluidic device represent the  
476 grains. Pore and grain sizes were designed to be 75, 150 and 300  $\mu\text{m}$ , corresponding to  
477 the range found in natural soil environments (54). In order to obtain comparable flow  
478 velocity conditions, the geometries were designed to have equal overall porosity (0.77).  
479 The initial fluid flow field in each porous geometry was computed using a 2D  
480 mathematical model that included an additional term to take drag forces in the third  
481 dimension into account (60). The model provided the velocities, and the shear rates  
482 were computed from the spatial derivative of the simulated fluid velocity field. The  
483 combination of three different pore sizes and four fluid flow rates (0.2, 0.5, 1 and 2 mL/h)  
484 allowed us to study twelve geometric and hydrodynamic experimental conditions.

485 **Microfluidic device fabrication.** The microfluidic devices were fabricated using  
486 standard soft lithography techniques. Microchannel molds were prepared by depositing  
487 SU-8 photoresist (MicroChem Corp., Newton, MA) on a silicon wafer via  
488 photolithography. The mold was silanized with trichloromethylsilane (Sigma Aldrich) prior  
489 to use. Microfluidic devices were prepared with a 10% w/w cross-linking agent in the  
490 PDMS solution (Sylgard 184 Silicone Elastomer Kit, Dow Corning, Midland, MI). Devices  
491 were cured at 80 °C for 2 h and plasma-bonded to a clean glass slide.

492 **Bacterial cultures.** Experiments were performed using wild-type *Bacillus subtilis* NCIB  
493 3610 as model organism. *B. subtilis* is a ubiquitous soil microbe, found predominantly on  
494 plant roots where it provides protection against plant pathogens. It is a well-studied  
495 biofilm former (11, 36, 61). The biofilm grown under flow presents a porous internal  
496 structure (14).

497 *B. subtilis* solutions were prepared by inoculating 3 mL nutrient solution n°3 (Sigma  
498 Aldrich) [meat extract 1 g/L, peptone 5g/L, NaCl 5 g/L, yeast extract 2 g/L] from a frozen  
499 bacterial stock and incubating overnight at 30 °C, while shaking at 200 rpm. Before  
500 experiments, the solution was diluted 1:1000 into fresh nutrient solution and incubated  
501 under the same conditions for 4 h to early exponential phase ( $\text{OD}_{600} = 0.1$ ), ensuring  
502 motile cells and minimizing cluster formation.

503 **Microfluidic assays.** Flow of nutrient solution (the same as that used for bacterial  
504 culture) was driven by a Harvard syringe pump at fluid flow rates 0.2, 0.5, 1 and 2 mL/h.  
505 Prior to use, all microfluidic devices were washed with 2 mL nutrient solution, then 150  
506  $\mu\text{L}$  (approximately the volume of the connecting tubes and the microfluidic device) of  
507 bacterial suspension was loaded into the microfluidic device by reversing the flow. A  
508 sterile filter (pore size 1.2  $\mu\text{m}$ ) separated the microfluidic device from the syringe to avoid  
509 bacterial contamination of the nutrient solution. After 3 h incubation to allow surface  
510 attachment of the cells, the flow was started. Biofilm growth and behavior was imaged  
511 for a period of 48 h at 25 °C. Imaging was performed on an inverted microscope (Ti-

512 Eclipse 2, Nikon, Japan) using a digital camera (Orca, Hamamatsu, Japan). Time-lapse  
513 images were acquired using bright-field microscopy ( $13500 \times 2500$  pixels at  $4\times$   
514 magnification, 1 frame per 6 min) in an array of 16 positions spanning the entire porous  
515 domain of the microfluidic device. A pressure sensor (Elveflow, France) recorded the  
516 pressure drop caused by the biofilm. The initial pressure was measured upstream of the  
517 porous medium prior to biofilm growth and manually set to zero in the recording  
518 software.

519 To study PFP behavior in the absence of cell growth, an experiment was performed in  
520 which the nutrient solution was replaced by an isotonic NaCl (Sigma Aldrich) solution.  
521 After 48 h of biofilm growth during which PFP intermittency was observed, the nutrient  
522 flow was exchanged for salt flow (NaCl 5 g/L) by switching through a Y-connector. All  
523 other parameters were kept constant. The porous domain was imaged for a further 24 h,  
524 together with a second domain exposed to continued flow of nutrient solution over the  
525 same period.

526 To capture the opening behavior of an individual PFP at high temporal resolution, a  
527 region was imaged at  $10\times$  magnification in phase contrast at 20 frames per second for 1  
528 hour during an ongoing experiment (with flow rate 1 mL/h and pore size 300  $\mu\text{m}$ ).

529 **Image analysis, statistics and derivations.** To obtain an image of the entire porous  
530 domain, images of the array of positions were stitched using Fiji ImageJ (62). All further  
531 image analysis was performed in MATLAB (MathWorks) using an in-house algorithm.  
532 Experimental replicates (1–4) were carried out for each combination of pore size and  
533 flow rate, with a greater number for the scenarios in which PFP formation and  
534 intermittency were observed (numbers of replicates are provided in *SI Appendix*, Table  
535 S1). All images were normalized by the mean intensity of the pillars and were binarized  
536 with a threshold of 0.3 in order to segment the image and differentiate biofilm from void  
537 space. The individual pore clogging speed was quantified by evaluating the change over  
538 time in the number of pixels allocated to the biofilm, measured along the shortest line  
539 transect between two pillars. As pore clogging is a bacterial growth process, the  
540 Gompertz model, typically used to model bacterial growth, can be fitted to the “clogging  
541 curve” (42), Eq. 3, and the maximal pore clogging speed extracted from the model  
542 (corresponding to the maximal growth rate of bacterial cultures). The corresponding  
543 Gompertz model is

$$y = A \cdot \exp \left\{ -\exp \left[ v_c \cdot \frac{\exp(1)}{A} (\lambda - t) + 1 \right] \right\}, \quad \text{EQ. 3}$$

544 with  $\lambda$  the lag time,  $v_c$  the maximum individual pore clogging speed, and  $A$  the maximum  
545 value of the asymptote. The fitted clogging curves and the distribution of individual pore  
546 clogging speeds are shown in the supplementary material (*SI Appendix*, Figs. S8 and  
547 S9). Goodness of fit and the obtention of physically realistic values were confirmed prior  
548 to computing the mean pore clogging speed. Only data from growth curves with a  
549 coefficient of determination  $R^2 > 0.98$  were retained in our calculation of the  
550 corresponding individual pore clogging speed,  $v_c$ . The number of pores evaluated for  
551 each experiment is given in the supplementary material (*SI Appendix*, Table S4).

552 The mean PFP width was obtained by computing the Euclidean distance in the PFP and  
553 calculating the mean PFP width per image (the number of measures depends on the  
554 length of the PFP expressed in pixels). The average PFP closing speed was quantified

555 based on linear interpolation from open state (maximal PFP width) to closed state  
556 (minimal PFP width) in the PFP width data (*SI Appendix*, Fig. S11). Opening frequency  
557 was estimated based on the time scale of opening events, calculated as the inverse of  
558 the time between two opening events. The Monod kinetics were fitted to the individual  
559 pore clogging speeds and PFP closing speeds using least squares regression. To track  
560 biofilm movement during PFP opening (*SI Appendix*, Movie S1), digital image correlation  
561 (DIC), adapted from (33), was computed using the PIVlab tool in MATLAB (MathWorks).  
562 DIC provided information about the direction of movement and detachment of the biofilm  
563 during PFP opening by tracking and cross-correlating changes in the image and  
564 therefore allowed identification of physical processes involved.

565  
566 **Acknowledgments**  
567

568 The authors acknowledge support from SNSF PRIMA grant 179834 (to E.S.), the US  
569 National Science Foundation grant EAR-1752982 (to F.J.C. and I.C.B.), discretionary  
570 funding from ETH (to R.S.), the Swiss National Science Foundation National Centre of  
571 Competence in Research (NCCR) Microbiomes (No. 51NF40\_180575 to R.S.), an ETH  
572 Zurich Research Grant (to R.S. and J.J.M.), and discretionary funding from Eawag (to  
573 J.J.M.).

574  
575 **References**  
576

- 577 1. A. B. Cunningham, R. R. Sharp, R. Hiebert, G. James, Subsurface biofilm barriers for the  
578 containment and remediation of contaminated groundwater. *Bioremediat. J.* **7**, 151–164  
579 (2003).
- 580 2. T. L. Stewart, H. Scott Fogler, Pore-scale investigation of biomass plug development and  
581 propagation in porous media. *Biotechnol. Bioeng.* **77**, 577–588 (2002).
- 582 3. P. Baveye, P. Vandevivere, B. L. Hoyle, P. C. DeLeo, D. Sanchez De Lozada,  
583 Environmental impact and mechanisms of the biological clogging of saturated soils and  
584 aquifer materials. *Crit. Rev. Environ. Sci. Technol.* **28**, 123–191 (1998).
- 585 4. J. K. Mitchell, J. C. Santamarina, Biological considerations in geotechnical engineering. *J.*  
586 *Geotech. Geoenvironmental Eng.* **131**, 1222–1233 (2005).
- 587 5. M. E. Davey, G. A. O'Toole, Microbial biofilms: from ecology to molecular genetics.  
588 *Microbiol. Mol. Biol. Rev.* **64**, 847–867 (2000).
- 589 6. H. C. Flemming, *et al.*, Biofilms: An emergent form of bacterial life. *Nat. Rev. Microbiol.* **14**,  
590 563–575 (2016).
- 591 7. H. C. Flemming, J. Wingender, The biofilm matrix. *Nat. Rev. Microbiol.* **8**, 623–633 (2010).
- 592 8. J. N. Wilking, T. E. Angelini, A. Seminara, M. P. Brenner, D. A. Weitz, Biofilms as complex  
593 fluids. *MRS Bull.* **36**, 385–391 (2011).
- 594 9. S. Kesel, *et al.*, Direct comparison of physical properties of *Bacillus subtilis* NCIB 3610  
595 and B-1 biofilms. *Appl. Environ. Microbiol.* **82**, 2424–2432 (2016).
- 596 10. C. J. Rupp, C. A. Fux, P. Stoodley, Viscoelasticity of *Staphylococcus aureus* biofilms in  
597 response to fluid shear allows resistance to detachment and facilitates rolling migration.  
598 *Appl. Environ. Microbiol.* **71**, 2175–2178 (2005).

599 11. A. Seminara, *et al.*, Osmotic spreading of *Bacillus subtilis* biofilms driven by an  
600 extracellular matrix. *Proc. Natl. Acad. Sci. U. S. A.* **109**, 1116–1121 (2012).

601 12. L. Prades, *et al.*, Computational and experimental investigation of biofilm disruption  
602 dynamics induced by high-velocity gas jet impingement. *MBio* **11**, e02813-19 (2020).

603 13. J. N. Wilking, *et al.*, Liquid transport facilitated by channels in *Bacillus subtilis* biofilms.  
604 *Proc. Natl. Acad. Sci.* **110**, 848–852 (2013).

605 14. L. Gierl, K. Stoy, A. Faíña, H. Horn, M. Wagner, An open-source robotic platform that  
606 enables automated monitoring of replicate biofilm cultivations using optical coherence  
607 tomography. *npj Biofilms Microbiomes* **6**, 18 (2020).

608 15. R. Rusconi, S. Lecuyer, L. Guglielmini, H. A. Stone, Laminar flow around corners triggers  
609 the formation of biofilm streamers. *J. R. Soc. Interface* **7**, 1293–1299 (2010).

610 16. H. C. Flemming, S. Wuertz, Bacteria and archaea on Earth and their abundance in  
611 biofilms. *Nat. Rev. Microbiol.* **17**, 247–260 (2019).

612 17. H. Vlamakis, Y. Chai, P. Beauregard, R. Losick, R. Kolter, Sticking together: Building a  
613 biofilm the *Bacillus subtilis* way. *Nat. Rev. Microbiol.* **11**, 157–168 (2013).

614 18. P. Thomen, *et al.*, Bacterial biofilm under flow: First a physical struggle to stay, then a  
615 matter of breathing. *PLoS One* **12**, e0175197 (2017).

616 19. H. Horn, H. Reiff, E. Morgenroth, Simulation of growth and detachment in biofilm systems  
617 under defined hydrodynamic conditions. *Biotechnol. Bioeng.* **81**, 607–617 (2003).

618 20. E. Secchi, *et al.*, The effect of flow on swimming bacteria controls the initial colonization of  
619 curved surfaces. *Nat. Commun.* **11**, 2851 (2020).

620 21. D. Scheidweiler, H. Peter, P. Pramateftaki, P. de Anna, T. J. Battin, Unraveling the  
621 biophysical underpinnings to the success of multispecies biofilms in porous environments.  
622 *ISME J.* **13**, 1700–1710 (2019).

623 22. A. Creppy, E. Clément, C. Douarche, M. V. D'Angelo, H. Auradou, Effect of motility on the  
624 transport of bacteria populations through a porous medium. *Phys. Rev. Fluids* **4**, 013102  
625 (2019).

626 23. J. A. Aufrecht, *et al.*, Pore-scale hydrodynamics influence the spatial evolution of bacterial  
627 biofilms in a microfluidic porous network. *PLoS One* **14**, e0218316 (2019).

628 24. P. Stoodley, I. Dodds, J. D. Boyle, H. M. Lappin-Scott, Influence of hydrodynamics and  
629 nutrients on biofilm structure. *J. Appl. Microbiol.* **85**, 19S–28S (1998).

630 25. C. D. Nadell, D. Ricarde, J. Yan, K. Drescher, B. L. Bassler, Flow environment and matrix  
631 structure interact to determine spatial competition in *Pseudomonas aeruginosa* biofilms.  
632 *Elife* **6**, e21855 (2017).

633 26. M. Peszynska, A. Trykozko, G. Iltis, S. Schlueter, D. Wildenschild, Biofilm growth in  
634 porous media: Experiments, computational modeling at the porescale, and upscaling. *Adv.*  
635 *Water Resour.* **95**, 288–301 (2016).

636 27. A. B. Cunningham, W. G. Characklls, F. Abedeen, D. Crawford, Influence of biofilm  
637 accumulation on porous media hydrodynamics. *Environ. Sci. Technol.* **25**, 1305–1311  
638 (1991).

639 28. R. R. Sharp, P. Stoodley, M. Adgie, R. Gerlach, A. Cunningham, Visualization and  
640 characterization of dynamic patterns of flow, growth and activity of biofilms growing in  
641 porous media. *Water Sci. Technol.* **52**, 85–90 (2005).

642 29. S. Bottero, *et al.*, Biofilm development and the dynamics of preferential flow paths in  
643 porous media. *Biofouling* **29**, 1069–1086 (2013).

644 30. W. M. Durham, O. Tranzer, A. Leonbruni, R. Stocker, Division by fluid incision: Biofilm  
645 patch development in porous media. *Phys. Fluids* **24**, 091107 (2012).

646 31. J. Jiménez-Martinez, T. Le Borgne, H. Tabuteau, Y. Méheust, Impact of saturation on  
647 dispersion and mixing in porous media: Photobleaching pulse injection experiments and  
648 shear-enhanced mixing model. *Water Resour. Res.* **53**, 1457–1472 (2017).

649 32. Y. A. Cengel, J. M. Cimbala, *Fluid Mechanics: Fundamentals and Applications* (2018).

650 33. J. D. Mathias, P. Stoodley, Applying the digital image correlation method to estimate the  
651 mechanical properties of bacterial biofilms subjected to a wall shear stress. *Biofouling* **25**,  
652 695–703 (2009).

653 34. F. J. Carrillo, I. C. Bourg, A Darcy-Brinkman-Biot approach to modeling the hydrology and  
654 mechanics of porous media containing macropores and deformable microporous regions.  
655 *Water Resour. Res.* **55**, 8096–8121 (2019).

656 35. F. J. Carrillo, I. C. Bourg, Modeling multiphase flow within and around deformable porous  
657 materials: A Darcy-Brinkman-Biot Approach. *Water Resour. Res.* **57**, e2020WR028734  
658 (2020).

659 36. J. Dervaux, J. C. Magniez, A. Libchaber, On growth and form of *Bacillus subtilis* biofilms.  
660 *Interface Focus* **4**, 20130051 (2014).

661 37. N. A. Mortensen, F. Okkels, H. Bruus, Reexamination of Hagen-Poiseuille flow: Shape  
662 dependence of the hydraulic resistance in microchannels. *Phys. Rev. E* **71**, 057301  
663 (2005).

664 38. S. Whitaker, Flow in porous media I: A theoretical derivation of Darcy's law. *Transp.  
665 Porous Media* **1**, 3–25 (1986).

666 39. J. Monod, The growth of bacterial cultures. *Annu. Rev. Microbiol.* **3**, 371–394 (1949).

667 40. M. Mehdi Salek, S. M. Jones, R. J. Martinuzzi, The influence of flow cell geometry related  
668 shear stresses on the distribution, structure and susceptibility of *Pseudomonas*  
669 *aeruginosa* 01 biofilms. *Biofouling* **25**, 711–725 (2009).

670 41. E. Paul, J. C. Ochoa, Y. Pechaud, Y. Liu, A. Liné, Effect of shear stress and growth  
671 conditions on detachment and physical properties of biofilms. *Water Res.* **46**, 5499–5508  
672 (2012).

673 42. M. H. Zwietering, I. Jongenburger, F. M. Rombouts, K. Van't Riet, Modeling of the  
674 bacterial growth curve. *Appl. Environ. Microbiol.* **56**, 1875–1881 (1990).

675 43. Y. P. Tsai, Impact of flow velocity on the dynamic behaviour of biofilm bacteria. *Biofouling*  
676 **21**, 267–277 (2005).

677 44. A. Siryaporn, M. K. Kim, Y. Shen, H. A. Stone, Z. Gitai, Colonization, competition, and  
678 dispersal of pathogens in fluid flow networks. *Curr. Biol.* **25**, 1201–1207 (2015).

679 45. P. de Anna, A. A. Pahlavan, Y. Yawata, R. Stocker, R. Juanes, Chemotaxis under flow  
680 disorder shapes microbial dispersion in porous media. *Nat. Phys.* **17**, 68–73 (2021).

681 46. P. Stoodley, Z. Lewandowski, J. D. Boyle, H. M. Lappin-Scott, Structural deformation of  
682 bacterial biofilms caused by short-term fluctuations in fluid shear: An in situ investigation  
683 of biofilm rheology. *Biotechnol. Bioeng.* **65**, 83–92 (1999).

684 47. I. Klapper, C. J. Rupp, R. Cargo, B. Purvedorj, P. Stoodley, Viscoelastic fluid description  
685 of bacterial biofilm material properties. *Biotechnol. Bioeng.* **80**, 289–296 (2002).

686 48. R. C. Grabowski, I. G. Droppo, G. Wharton, Erodibility of cohesive sediment: The  
687 importance of sediment properties. *Earth-Science Rev.* **105**, 101–120 (2011).

688 49. M. Zhang, G. Yu, Critical conditions of incipient motion of cohesive sediments. *Water  
689 Resour. Res.* **53**, 7798–7815 (2017).

690 50. E. Vignaga, *et al.*, Erosion of biofilm-bound fluvial sediments. *Nat. Geosci.* **6**, 770–774  
691 (2013).

692 51. T. Shaw, M. Winston, C. J. Rupp, I. Klapper, P. Stoodley, Commonality of elastic  
693 relaxation times in biofilms. *Phys. Rev. Lett.* **93**, 1–4 (2004).

694 52. H. Kitamura, T. Omori, T. Ishikawa, Impact of rheological properties on bacterial streamer  
695 formation. *J. R. Soc. Interface* **18** (2021).

696 53. K. Z. Coyte, H. Tabuteau, E. A. Gaffney, K. R. Foster, W. M. Durham, Microbial  
697 competition in porous environments can select against rapid biofilm growth. *Proc. Natl.  
698 Acad. Sci.* **114**, E161–E170 (2017).

699 54. R. Taylor, A. Cronin, S. Pedley, J. Barker, T. Atkinson, The implications of groundwater  
700 velocity variations on microbial transport and wellhead protection - Review of field  
701 evidence. *FEMS Microbiol. Ecol.* **49**, 17–26 (2004).

702 55. M. K. Nassar, *et al.*, Large-scale experiments in microbially induced calcite precipitation  
703 (MICP): reactive transport model development and prediction. *Water Resour. Res.* **54**,  
704 480–500 (2018).

705 56. C. Wu, J. Chu, S. Wu, L. Cheng, L. A. van Paassen, Microbially induced calcite  
706 precipitation along a circular flow channel under a constant flow condition. *Acta Geotech.*  
707 **14**, 673–683 (2019).

708 57. C. Dreszer, H. C. Flemming, A. Zwijnenburg, J. C. Kruithof, J. S. Vrouwenvelder, Impact  
709 of biofilm accumulation on transmembrane and feed channel pressure drop: Effects of  
710 crossflow velocity, feed spacer and biodegradable nutrient. *Water Res.* **50**, 200–211  
711 (2014).

712 58. A. Sternagel, R. Loritz, J. Klaus, B. Berkowitz, E. Zehe, Simulation of reactive solute  
713 transport in the critical zone: A Lagrangian model for transient flow and preferential  
714 transport. *Hydrol. Earth Syst. Sci.* **25**, 1483–1508 (2021).

715 59. Y. Yawata, J. Nguyen, R. Stocker, Microfluidic Studies of Biofilm Formation in Dynamic  
716 Environments. *J. Bacteriol.* **198**, 2589–2595 (2016).

717 60. A. Ferrari, J. Jimenez-Martinez, T. Le Borgne, Y. Méheust, I. Lunati, Challenges in  
718 modeling unstable two-phase flow experiments in porous micromodels. *Water Resour.  
719 Res.* **51**, 1381–1400 (2015).

720 61. A. Dragoš, *et al.*, Division of labor during biofilm matrix production. *Curr. Biol.* **28**, 1903-  
721 1913.e5 (2018).

722 62. S. Preibisch, S. Saalfeld, P. Tomancak, Globally optimal stitching of tiled 3D microscopic  
723 image acquisitions. *Bioinformatics* **25**, 1463–1465 (2009).

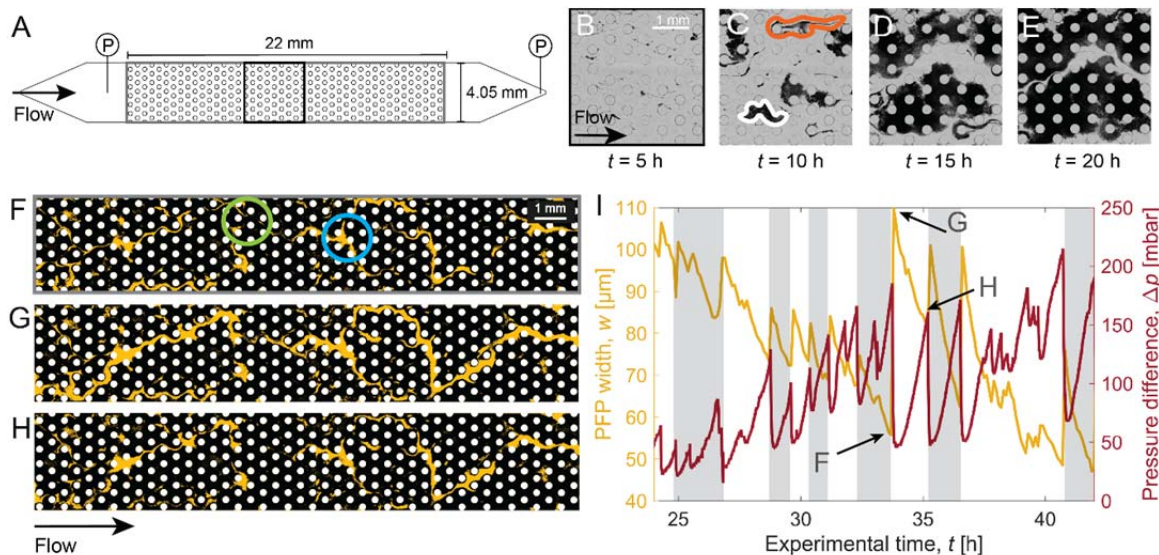
724 63. A. Karampatzakis, *et al.*, Probing the internal micromechanical properties of  
725 *Pseudomonas aeruginosa* biofilms by Brillouin imaging. *npj Biofilms Microbiomes* **3**, 20  
726 (2017).

727

728

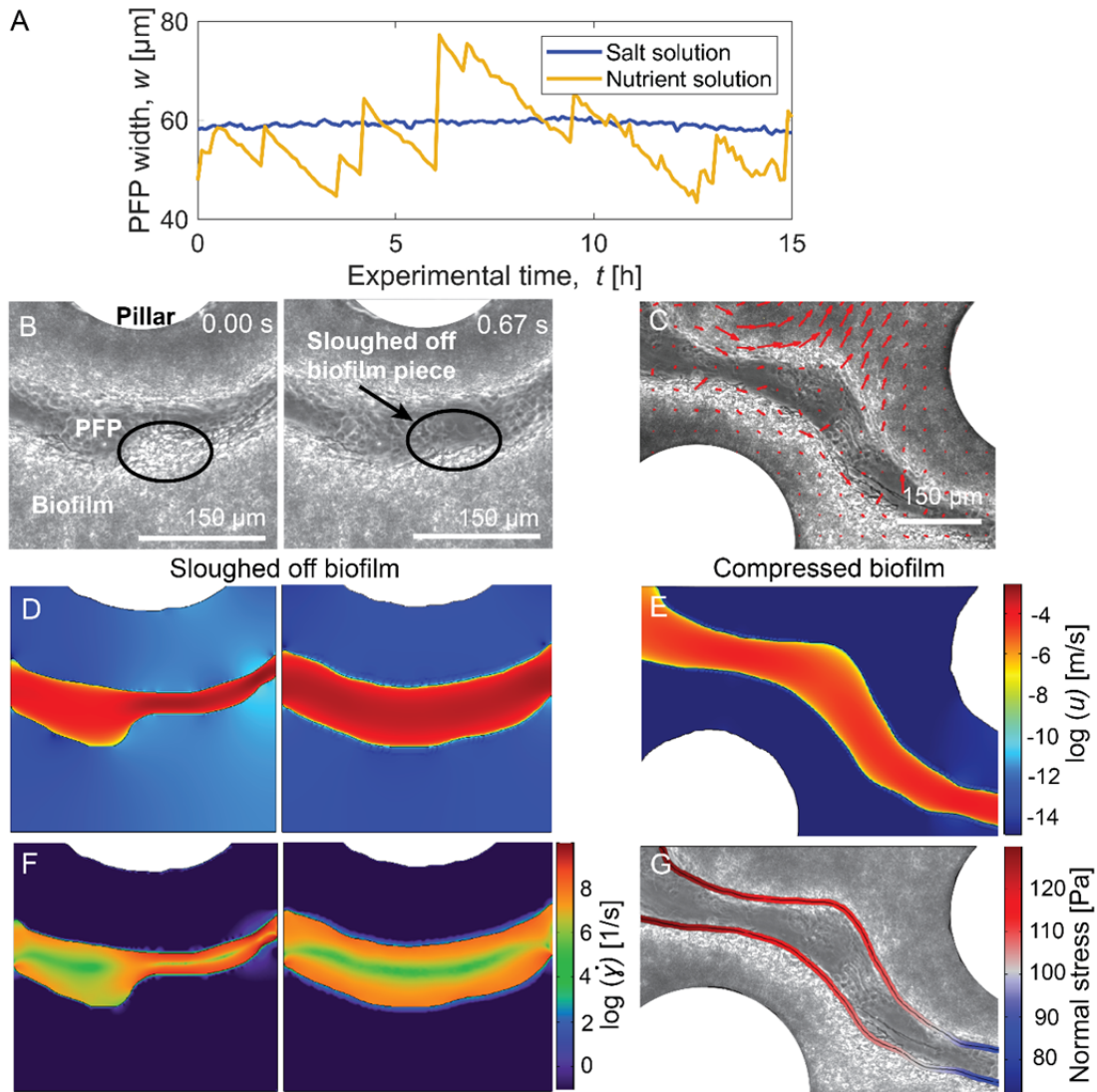
729 **Figures and Tables**

730  
731



732  
733 **Fig. 1.** Preferential flow path (PFP) formation and intermittency in a model porous  
734 medium. Fluid flow rate = 1 mL/h. (A) Schematic of the microfluidic device showing the  
735 porous domain (height  $h = 100 \mu\text{m}$ ; pore size  $d = 300 \mu\text{m}$ ) and locations of the pressure  
736 sensors (P). (B–E) Bright-field time-lapse images of biofilm formation, from initial  
737 attachment (B), through the formation of streamers (orange outline) and clusters (white  
738 outline) (C), to near clogging (D and E). (F–H) Segmented images of the porous medium  
739 at three points in time, showing the pillars (white), biofilm (black) and PFPs (yellow). The  
740 images were taken at times  $t = 33.7 \text{ h}$  (F),  $t = 33.8 \text{ h}$  (G),  $t = 35.2 \text{ h}$  (H), with the recorded  
741 pressure difference  $\Delta p = 185 \text{ mbar}$  (F),  $\Delta p = 50 \text{ mbar}$  (G),  $\Delta p = 160 \text{ mbar}$  (H). Closing  
742 PFPs have a narrow width (F and H), while open PFPs have a larger width (G). PFPs  
743 can branch (blue circle) and coalesce (green circle). (I) Mean PFP width,  $w$ , (yellow  
744 curve) and pressure difference,  $\Delta p$ , (red curve) across the entire porous domain as a  
745 function of time. Gray bars indicate every second cycle of rapid PFP opening and  
746 gradual PFP closing. An opening event was defined to occur at a PFP width change of 5  
747  $\mu\text{m}$ . Biofilm behavior causes a decrease in pressure difference across the porous  
748 domain when PFPs open and an increase in pressure difference when PFPs close. For  
749 example, narrowing of the PFPs by 27  $\mu\text{m}$  over a period of 1.4 h (G to H) increases the  
750 pressure difference by 110 mbar, and very rapid widening of the PFPs by 54  $\mu\text{m}$   
751 decreases the pressure difference by 135 mbar (F to G). Letters correspond to the  
752 experimental images in F–H. Note that the pressure difference for the initial biofilm-free  
753 porous domain at the imposed fluid flow rate was subtracted, in order to isolate the  
754 impact of the biofilm on the pressure difference.

755  
756

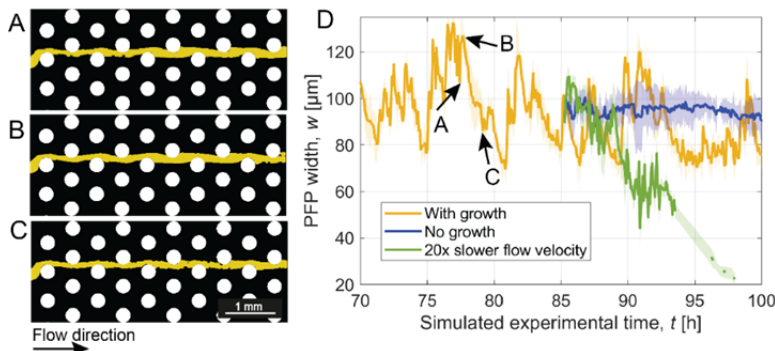


757  
758

759 **Fig. 2.** In the intermittency observed in preferential flow paths, PFP closing is driven by  
760 microbial growth, while PFP opening is driven by hydrodynamically induced stresses on  
761 the biofilm. (A) For a mature biofilm, replacing the flowing nutrient solution with a  
762 nutrient-free salt solution causes the intermittency in the PFP width to cease (blue  
763 curve), in comparison with continued intermittency under constant nutrient flow (yellow  
764 curve). This demonstrates that PFP closing is driven by microbial growth. Before data  
765 collection, biofilms were allowed to develop for 24 h, and the solution within the porous  
766 medium was allowed to equilibrate for 2 h after the change to a salt solution, before flow  
767 was resumed. Bright-field image sequences of the biofilms corresponding to this data  
768 are shown in *S/ Appendix*, Fig. S4. (B) Images acquired in rapid sequence during PFP  
769 opening, showing the detachment of a portion of the biofilm (area  $\sim 3600 \mu\text{m}^2$ ) adjacent  
770 to the PFP. The black ellipse indicates the location of the sloughed off biofilm. (C) Digital  
771 image correlation analysis of high-speed videos showing biofilm movement during PFP  
772 opening through compression of the biofilm structure. Red arrows indicate local  
773 movement within the biofilm mostly normal to the PFP, with larger arrows signifying a

774 larger local biofilm movement. (*D, E*) Numerically computed fluid velocity  $u$  (note  
775 logarithmic color scale) for the geometries corresponding to the images in panels B and  
776 C, showing higher velocities in the narrower PFP regions. (*F*) Shear rate (note  
777 logarithmic color scale) computed from the numerical velocity field. Shear rates next to  
778 the PFP boundaries are much higher in a narrow path compared to an open path. (*G*)  
779 The stress normal to the PFP boundaries, obtained from the numerical simulations.  
780  
781

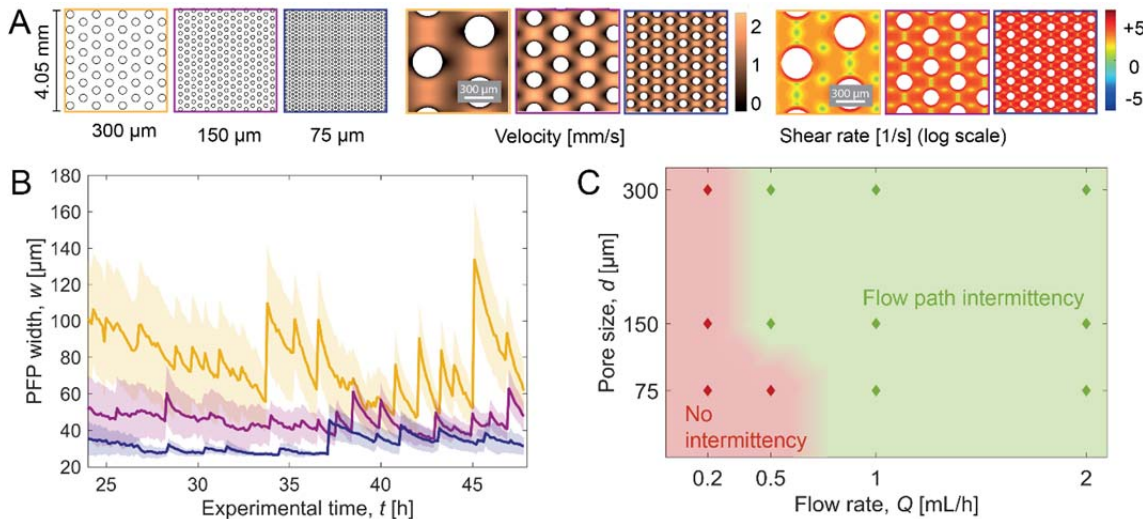
782  
783



784 Fig. 3. A model of biofilm formation and behavior in flow predicts that PFP intermittency  
785 is dependent on microbial growth and fluid flow velocity. (A–C) Simulated biofilm growth  
786 and PFP intermittency, similar to experimental images in Fig. 1 F–H. The segmented  
787 images represent the simulation of a porous domain of  $5 \times 2$  mm at time points  $t = 77.4$   
788 h (A),  $t = 77.6$  h (B),  $t = 79.2$  h (C). PFPs are highlighted in yellow, biofilm is shown in  
789 black, and pillars are shown in white. The mathematical model was implemented using  
790 the same parameters and boundary conditions as the experimental setup (Fig. 1A), with  
791  $d = 300$   $\mu\text{m}$ ,  $h = 100$   $\mu\text{m}$ , porosity = 0.77, and fluid flow rate = 1 mL/h. Biofilm-related  
792 parameters such as kinematic viscosity =  $6.67 \times 10^{-6}$   $\text{m}^2/\text{s}$ , yield stress = 0.4 Pa, and  
793 permeability =  $2.2 \times 10^{-14}$   $\text{m}^2$  were taken from experimental measurements following  
794 existing protocols (SI Appendix). Biofilm density = 1200  $\text{kg}/\text{m}^3$  was obtained from the  
795 literature (63). A detailed description of the derivation of these parameters can be found  
796 in SI Appendix. (D) Predicted PFP width showed intermittency when microbial growth  
797 was included (yellow curve), but not when growth was excluded from the model (blue  
798 curve). A lower fluid flow rate of 0.05 mL/h (green line) induced a decrease in mean PFP  
799 width and subsequent disappearance of the PFPs. Letters correspond to the images in  
800 A–C. Shading indicates the error bars showing the standard deviation of PFP width.

801  
802

803



804

805

806

807

808

809

810

811

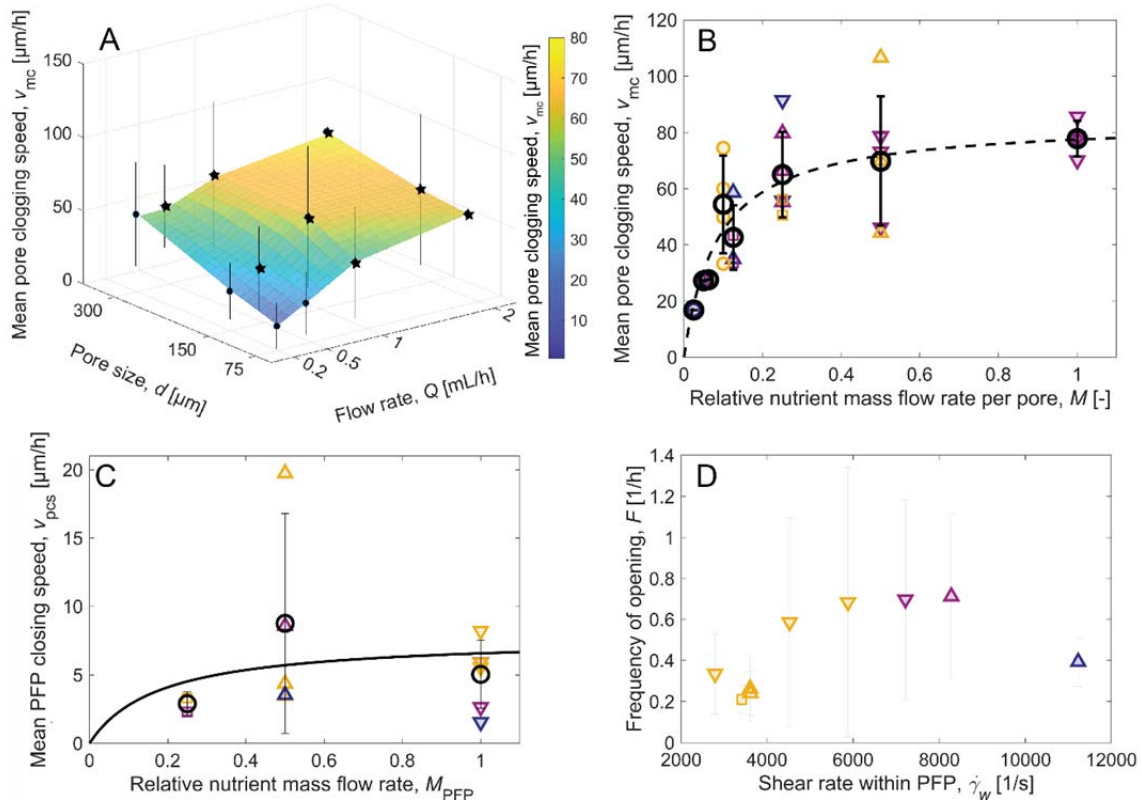
812

813

**Fig. 4.** PFP intermittency occurs at high flow velocities and large pore sizes. (A) Schematics of part of the porous domain showing the three pore sizes,  $d$ , considered in experiments (300  $\mu\text{m}$ , yellow; 150  $\mu\text{m}$ , purple; 75  $\mu\text{m}$ , blue) and magnified views of the initial velocity field and shear rate field before biofilm growth obtained from a mathematical model at fluid flow rate,  $Q = 1 \text{ mL/h}$ . The porosity of all models is 0.77. (B) Time course of mean PFP width,  $w$ , for different pore sizes,  $d$  (color-coding as in A), for a fluid flow rate of  $Q = 1 \text{ mL/h}$ . Shading indicates the standard deviation of  $w$  computed over the length of the PFPs. (C) Phase diagram for PFP intermittency in experiments as a function of pore size and fluid flow rate.

814

815



816  
 817 **Fig. 5.** Bioclogging of porous media and PFP closing speeds depend on the nutrient  
 818 mass flow, while the frequency of PFP opening depends on the average shear rate  
 819 within PFPs. (A) Mean pore clogging speed,  $v_{mc}$ , depends on the pore size,  $d$ , and the  
 820 fluid flow rate,  $Q$ . Data points (black) represent the mean of experimental replicates (SI  
 821 Appendix, Table S1) and error bars the standard deviation. The plane was fitted by  
 822 linear interpolation, colored according to values of  $v_{mc}$ . Stars indicate conditions in which  
 823 PFP intermittency was observed. (B) The relationship between nutrient mass flow per  
 824 pore,  $M$ , and the mean pore clogging speed,  $v_{mc}$ , follows a Monod kinetic (dashed line).  
 825 Mean values of  $v_{mc}$  for each nutrient mass flow rate are shown as black circles with their  
 826 corresponding standard deviation. Values of  $v_{mc}$  are also shown for each experimental  
 827 combination of fluid flow rate (symbols: circle, 0.2  $\text{mL}/\text{h}$ ; square, 0.5  $\text{mL}/\text{h}$ ; upward-  
 828 pointing triangle, 1  $\text{mL}/\text{h}$ ; downward-pointing triangle, 2  $\text{mL}/\text{h}$ ) and pore size (colors:  
 829 yellow, 300  $\mu\text{m}$ ; purple, 150  $\mu\text{m}$ ; blue, 75  $\mu\text{m}$ ). The fitted parameters for the Monod  
 830 kinetic equation (Eq. 1) are  $v_{mc,\text{max}} = 84.13 \mu\text{m}/\text{h}$  and  $K_N \cdot Q = 0.086$ . (C) The relationship  
 831 between the relative nutrient mass flow rate,  $M_{PFP}$ , and the mean PFP closing speed,  $v_{pos}$ ,  
 832 follows a Monod kinetic (solid line) with fitted parameters of the Monod equation  $v_{pos,\text{max}} =$   
 833 7.75  $\mu\text{m}/\text{h}$  and  $K_N \cdot Q = 0.178$ . For this analysis, the nutrient mass flow rate in the PFPs,  
 834  $M_{PFP}$ , was assumed proportional to the imposed fluid flow rate. Circles represent the  
 835 mean for each nutrient mass flow rate and bars represent the standard deviation. Other  
 836 symbols show the values for individual experimental combinations of fluid flow rate and  
 837 pore size, with symbols and colors as in B. (D) The frequency of opening,  $F$ , of the PFPs  
 838 increases with the shear rate,  $\dot{\gamma}_w$ . Shear rate within the PFPs was estimated from the  
 839 flow rate and mean PFP dimensions (Results). Data are shown for each combination of  
 840 fluid flow rate and pore size (symbols and colors as in B). Only data from experiments  
 841 with more than one opening event were used to determine the frequencies.

